Computers in Biology and Medicine 114 (2019) 103453

Contents lists available at ScienceDirect

Computers in Biology and Medicine

journal homepage: www.elsevier.com/locate/compbiomed

Endothelium resolving simulations of wall shear-stress dependent mass transfer of LDL in diseased coronary arteries

S. Kenjereš *, J.P. van der Krieke, C. Li

Transport Phenomena Section, Department of Chemical Engineering, Faculty of Applied Sciences and J. M. Burgerscentrum for Fluid Mechanics, Delft University of Technology, Van der Maasweg 9, 2629 HZ Delft, The Netherlands

ARTICLE INFO

Keywords:
CFD
Coronary artery
Blood flow
Mass transfer
LDL
hypertension
stenosis

ABSTRACT

In the present study, we investigate blood flow and mass transfer of the low-density lipoprotein (LDL) in a simplified axisymmetric geometry with a mathematically well-defined narrowing (stenosis), which mimics a diseased human coronary artery. The interior of the arterial wall is represented as a porous media containing multi-layered structures of different thickness. This multi-layered structure includes anatomically realistic sublayers: endothelium, intima, internal elastic layer (IEL), media and adventitia. The coupling between the blood flow and mass transfer of LDL in the lumen (interior of artery) and arterial wall is established through a multipore model at the lumen/endothelium interface. This multipore model takes into consideration three different contributions for transport of LDL: normal and leaky junctions of endothelial cells, as well as their vesicular pathway. A comprehensive mathematical model, which is based on solving the set of PDEs for conservation of mass, momentum, and concentration, is completed by introducing the wall shear-stress (WSS) dependent transport properties of the arterial wall. Several variants of the model are evaluated, including the constant and wall shear-stress dependent transport properties of the endothelium, as well as different representation of the arterial wall internal structure. The response of the model on changing the transmural pressure (to simulate hypertension effects) and geometrical shapes of the stenosis (to mimic the various stages of atherosclerosis development) is also presented. It is shown that the present model can predict the levels of LDL inside the arterial wall in good agreement with experimental studies in pressurized rabbit aorta under similar conditions. The model is recommended for future simulations of LDL accumulation in the patient-specific cardiovascular system conditions.

1. Introduction

Atherosclerotic cardiovascular disease remains the leading cause of death and disability in the United States and Europe, [1–4]. As such it is of great importance to understand the fundamental causes of disease development to be able to prevent and cure it more effectively. Atherosclerosis is an inflammatory disease, characterized by endothelial dysfunction and the buildup of lipids, cholesterol, calcium and cellular debris within the arterial wall of large and medium-sized muscular arteries, [5]. It is postulated that this endothelial dysfunction is caused by elevated LDL-cholesterol concentration, hypertension, obesity, diabetes, smoking, physical inactivity, etc., [6]. Development of atherosclerosis starts with the accumulation of lipoprotein in macrophages in the intima sublayer of an arterial wall. This accumulation results in visible fatty streaks, which are the first pathologic lesions of atherosclerosis. As lipids and cholesterol are provided by low density lipoprotein (LDL), and without adequate removal from the macrophages by functional high density lipoprotein (HDL), the lesions grow, forming atheromatous plaques (as illustrated in Fig. 1, for a case of the left circumflex coronary artery). The presence of plaques triggers a cascade of events that results in clot enlargement, which may, with time, obstruct the flow of blood. A complete blockage leads to ischaemia of whatever organ the artery provides blood for. If the organ is heart or brain, this process is called a 'heart attack' or 'stroke' respectively, causing potentially life threatening damage, [7,8].

Of course, this is an overly simplified description of atherosclerosis. In reality, many of the underlying processes for the initiation of this disease are still unknown and are the topic of undergoing research worldwide. Despite the complexity of cardiovascular diseases, there is much clinical evidence that certain factors play a major role. These include elevated levels of the LDL and arterial pressure (hypertension) as well as the inflammation caused by the oxidized LDL within the arterial wall. In the present study, we will introduce a mathematical model based on the transport equation of the LDL, which includes

* Corresponding author.
E-mail address: s.kenjeres@tudelft.nl (S. Kenjereš).

https://doi.org/10.1016/j.compbiomed.2019.103453
Received 13 May 2019; Received in revised form 30 August 2019; Accepted 15 September 2019
Available online 17 September 2019

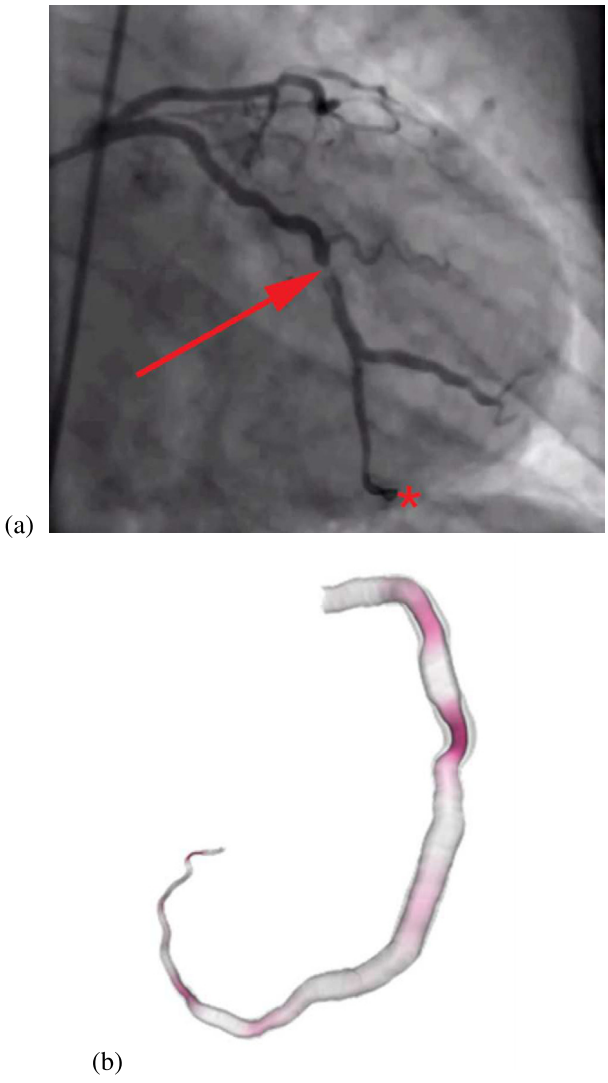

Fig. 1. Coronary angiography showing partial occlusion of the left circumflex coronary artery (as indicated by the red arrow) (a); The reconstructed geometry of the left circumflex coronary artery obtained by computed tomography angiography (CTA) (b). The red color denotes regions where the diameter is less than the (locally interpolated) average diameter (stenotic regions).
Source: Courtesy of Dr. T. van Walsum and Dr. H. A. Kirisli, Erasmus Medical Centre Rotterdam, The Netherlands.

all main transport mechanisms: convection, diffusion and biochemical reaction. In addition to the LDL, we also consider blood flow within the lumen (interior of an artery) as well as the plasma flow within a porous arterial wall — both described with modified Navier–Stokes equations. These modifications can include non-Newtonian effects for the blood flow, and porous wall effects (Darcy's law terms) for plasma flow.

Different models of LDL transport through an arterial wall have been proposed in literature. The simplest model is the wall-free model where only the interior of an artery is considered (lumen) and the effects of the surrounding wall are calculated through the imposed boundary conditions, [9,10]. The primary advantage of such a model is its simplicity, and the main deficiency is its inability to provide any information regarding plasma or LDL distribution within the arterial wall. The more complicated models also include the arterial wall as a homogeneous porous media layer, [11–13]. The most complicated model includes an anatomically realistic multi-layered structure of the arterial wall, [14–18]. This multi-layered structure includes the endothelium (with a typical thickness of ≈ 2 μm), intima (with a thickness of ≈ 10 μm), internal elastic layer (IEL) (with a thickness of ≈ 2 μm), media (with a thickness of ≈ 200 μm), and adventitia (with a thickness of ≈ 60–400 μm). In the present work, we will combine the multipore model of [11] with the multi-layered arterial wall structure. As a first step, we will introduce the model where the endothelium is treated separately from the rest of the arterial wall and will be numerically resolved. As a second step, the rest of the arterial wall will be not treated as a homogeneous layer, but as a multi-layered geometry which corresponds to the anatomic structure of the arterial wall, i.e. in addition to the endothelium, also the intima, the internal elastic layer (IEL), and the media will be numerically resolved. The major novelty of the present work is in the coupling of the multipore transport model of LDL across the lumen/endothelium interface with the multi-layered arterial wall structure, as well as the inclusion of the inflammation process.

The presented model represents a hybrid model that is constructed on the WSS dependent LDL transport of [11,12] (who considered only a single-layer arterial wall structure without resolving the endothelium), and the multi-layered arterial wall structure of [14,15] (who considered only constant transport properties of the endothelium). The similar approach was followed in [17], but they considered a fully developed flow in a simple cylinder with a single value of the transmural pressure and a constant filtration velocity (1D analysis).

Our final goal is to provide a mathematical model which is based on an anatomically realistic geometrical representation of the inner structure of the arterial wall and a sound physical foundation of the transport of LDL through the endothelial cells which involves three characteristic pathways: through normal junctions, through leaky junctions, and through vesicles. The final form of the model should also be suitable for patient-specific simulation of LDL accumulation in various parts of the human cardiovascular system.

2. Mathematical model

2.1. Arterial interior: lumen

The blood is assumed to be a homogeneous Newtonian fluid (which is valid for the considered here value of the Reynolds number, i.e. Re=$\mathcal{O}(10^2)$), with its behavior determined by conservation of mass and momentum as:

$$\nabla \cdot \vec{v}_{\mathrm{L}} = 0 \tag{1}$$

$$\rho_{\mathrm{B}} \frac{\partial \vec{v}_{\mathrm{L}}}{\partial t} + \rho_{\mathrm{B}} \left(\vec{v}_{\mathrm{L}} \cdot \nabla\right) \vec{v}_{\mathrm{L}} = -\nabla p_{\mathrm{L}} + \mu_{\mathrm{B}} \nabla^2 \vec{v}_{\mathrm{L}} \tag{2}$$

where ρ_{B} is the density and μ_{B} is the dynamic viscosity of the whole blood. The transport of the low-density lipoprotein (LDL) obeys the standard convection–diffusion transport equation, which can be written as:

$$\frac{\partial c_{\mathrm{LDL,L}}}{\partial t} + \vec{v}_{\mathrm{L}} \cdot \nabla c_{\mathrm{LDL,L}} = D_{\mathrm{L}} \nabla^2 c_{\mathrm{LDL,L}} \tag{3}$$

where the $D_{\mathrm{L}} = \nu/\mathrm{Sc}$ is the diffusion coefficient, ν is the kinematic viscosity and Sc is the Schmidt number.

2.2. Connecting the lumen and endothelium: WSS dependent wall properties

The multipore model connecting the lumen and endothelium assumes that the total momentum and concentration flux can be expressed as a sum of contributions through different pathways, [11,12,19]. These contributions include the normal ("nj") and leaky ("lj") junctions as well as the vesicular pathway ("vp"), and are calculated as:

$$J_{\mathrm{v}} = J_{\mathrm{v,nj}} + J_{\mathrm{v,lj}} + J_{\mathrm{v,vp}} \tag{4}$$

$$J_{\mathrm{s}} = J_{\mathrm{s,nj}} + J_{\mathrm{s,lj}} + J_{\mathrm{s,vp}} = \left(P_{\mathrm{nj}} + P_{\mathrm{lj}} + P_{\mathrm{vp}}\right) \Delta c_{\mathrm{LDL}}^{\mathrm{interface}} \tag{5}$$

$$\Delta c_{\mathrm{LDL}}^{\mathrm{interface}} = \left(c_{\mathrm{LDL,L}}^{\mathrm{endothelium}} - c_{\mathrm{LDL}}^{\mathrm{intima}}\right) \tag{6}$$

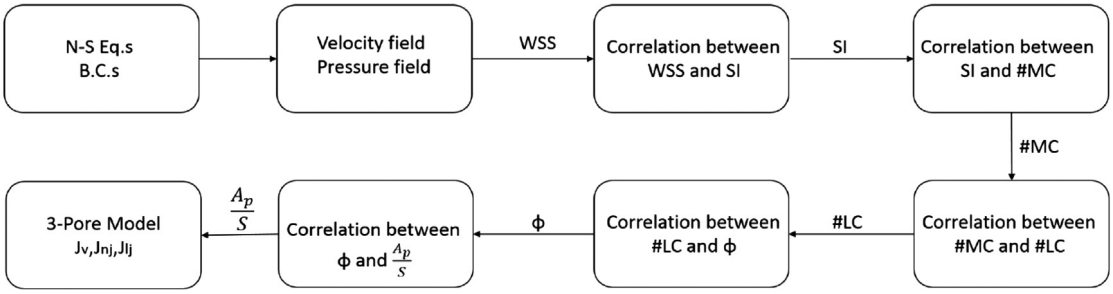

Fig. 2. Flow chart of the WSS-dependent endothelium properties of the model of [11].

where J_v is the total volume flux, J_s is the total concentration flux, P is the permeability, and $c_{\mathrm{LDL,L}}^{\mathrm{endothelium}}$ is the concentration of the LDL at the lumen side of the endothelium. For the volume flux, the vesicular pathway is much smaller than through the normal and leaky junctions. In contrast, the concentration flux occurs through leaky junctions and vesicular pathways, since the normal junctions prevent transport of macromolecules with radius larger than 2 nm. The total volume flux can now be written as:

$$J_{\mathrm{v}} = \left(L_{\mathrm{p,nj}} + L_{\mathrm{p,lj}}\right) \Delta p \tag{7}$$

where L_p is the hydraulic conductivity and Δp is the pressure drop across the endothelium. The hydraulic conductivity of the normal junctions is estimated to be $L_{\mathrm{p,nj}} = 1.16 \times 10^{-9}$ m/Pa s, [11]. Similarly, the value of the vesicular permeability $P_{\mathrm{vp}} = 1.92 \times 10^{-11}$ m/s, as reported in [20]. The hydraulic conductivity and diffusive permeability of the leaky junctions are defined as:

$$L_{\mathrm{p,lj}} = \frac{A_{\mathrm{p}}}{S} L_{\mathrm{p,slj}}, \quad P_{\mathrm{lj}} = \frac{A_{\mathrm{p}}}{S}\left(1 - \frac{r_{\mathrm{LDL}}}{w}\right) P_{\mathrm{slj}} \tag{8}$$

where A_{p}/S is the fraction of the surface areas S occupied by the leaky junctions, r_{LDL} is the radius of the LDL macromolecule (≈10 nm), w is the pore half-width (≈ 20 nm), $L_{\mathrm{p,slj}}$ is the hydraulic conductivity and P_{slj} is the diffusive permeability of a single leaky junction. The latter are calculated as:

$$L_{\mathrm{p,slj}} = \frac{w^2}{3\mu_{\mathrm{P}} l_{\mathrm{lj}}}, \quad P_{\mathrm{slj}} = \frac{D_{\mathrm{lj}}}{l_{\mathrm{lj}}} \tag{9}$$

where l_{lj} is the length of the leaky junction (same as the thickness of the endothelium, 2 μm), μ_{P} is the dynamic viscosity of plasma, and D_{lj} is the diffusion of the leaky junction. The diffusion of the leaky junction is related to the free diffusion coefficient in the lumen (D_{L}) as a function of the ratio of the radius of the transported molecule and the half-width of the leaky junction. For the transport of LDL, [21] reported that $D_{\mathrm{lj}} = 0.51 D_{\mathrm{L}}$. Similarly, the concentration drag coefficient of the leaky junction ($\sigma_{\mathrm{f,lj}}$) is also a function of the restrictive diffusivity and is estimated in accordance with [21] to be 0.55. Finally, to connect the total with contributions from a single leaking cell, we need to estimate the A_{p}/S ratio, as shown in Eq. (8). By applying the model of [11], this ratio can be simply evaluated as

$$\frac{A_{\mathrm{p}}}{S} = \frac{4w}{R_{\mathrm{cell}}}\phi \tag{10}$$

where R_{cell} is the radius of the leaky cell and ϕ is the fraction of leaky junctions. If the value of ϕ is known, all transport properties within the endothelium can be estimated. In the model of [11], the leaky junctions are modeled as ring-shaped pores surrounding leaky cells with a spacing of 2ξ. The fraction of leaky junctions is expressed as a ratio of the area of leaky cells and the area of all cells:

$$\phi \sim \frac{R_{\mathrm{cell}}^2}{\xi^2} \tag{11}$$

where R_{cell} is the endothelial cell radius (taken to be 15 μm, [22]), and ξ is the distance between the leaky cells which depends on the local flow characteristics. In the model of [11], the fraction of the leaky junctions is estimated through the following four steps process: (I) In the first step, the changes of the endothelial cells due to the wall shear-stress (calculated as $\tau_{\mathrm{w}} = \mu\,(\partial v/\partial r)|_{r=0}$) at the lumen/endothelium interface are represented through the shape index ($\mathrm{SI} = 4\pi \times \mathrm{area}/\,(\mathrm{perimeter})^2$). For a perfectly circular cell, the shape index is one, and for a very elongated cell, the shape index is zero. By calibrating the experimentally obtained shapes of the endothelial cells under various WSS conditions [11,23–26] adopted the following correlation:

$$\mathrm{SI} = 0.38 \cdot e^{-0.79 \cdot \mathrm{WSS}} + 0.225 \cdot e^{-0.043 \cdot \mathrm{WSS}} \tag{12}$$

(II) In the second step, the number of the mitotic cells is evaluated as a function of the shape index (SI), which is based on the experiments of [27], and can be written as:

$$\#\mathrm{MC} = 0.003797 \cdot e^{14.75 \cdot \mathrm{SI}} \tag{13}$$

(III) In the third step, based on experiments of [28], the number of leaky cells is expressed as a function of the number of mitotic cells as:

$$\#\mathrm{LC} = 0.307 + 0.805 \cdot \#\mathrm{MC} \tag{14}$$

(IV) Finally, the fraction of the leaky cells is evaluated [11] as:

$$\phi = \#\mathrm{LC}\frac{\pi R_{\mathrm{cell}}^2}{\text{unit area}} \tag{15}$$

It can be seen that by knowing ϕ, the ratio A_{P}/S can be calculated from Eq. (10), and consequently, Eq. (8) can be evaluated, making a fully closed system of equations connecting the WSS and transport properties of the endothelium. By re-arranging Eq. (7), we have:

$$L_{\mathrm{p,nj}} + L_{\mathrm{p,lj}} = \frac{J_v}{\Delta p} = \frac{K_{\mathrm{E}}}{\mu_p d} \tag{16}$$

where μ_p is the dynamic viscosity of plasma, d is the characteristic thickness of the endothelium and K_E is the Darcy's permeability of the endothelium. The latter is now a function of the hydraulic conductivity of the leaky junctions. Similarly, in analogy with Eq. (8), the effective diffusivity of the endothelium can be obtained as:

$$D_{\mathrm{E}} = \frac{A_{\mathrm{P}}}{S}\left(1 - \frac{r_{\mathrm{LDL}}}{w}\right) D_{\mathrm{lj}} \tag{17}$$

making it a function of the A_{P}/S ratio, and ultimately, a function of the WSS (through 'ϕ' dependency, Eqn.9). The flow chart of the WSS-dependent endothelium properties model (steps (I)–(IV)) is shown in Fig. 2.

The final form of the transport equation of the LDL concentration within the endothelium can be written as:

$$\frac{\partial \langle c_{\mathrm{LDL,E}} \rangle}{\partial t} + \left(1 - \sigma_{\mathrm{f,lj}}\right) \langle \vec{v}_{\mathrm{E,lj}} \rangle \cdot \nabla \langle c_{\mathrm{LDL,E}} \rangle = \nabla \cdot \left(\overline{\overline{D}}_{\mathrm{E}} \, \nabla \langle c_{\mathrm{LDL,E}} \rangle \right) \tag{18}$$

where $\langle \vec{v}_{\mathrm{E,lj}} \rangle$ is the velocity of plasma through the leaky junctions:

$$\langle \vec{v}_{\mathrm{E,lj}} \rangle = \frac{L_{\mathrm{p,lj}}}{L_{\mathrm{p,lj}} + L_{\mathrm{p,nj}}} \langle \vec{v}_{\mathrm{E}} \rangle \tag{19}$$

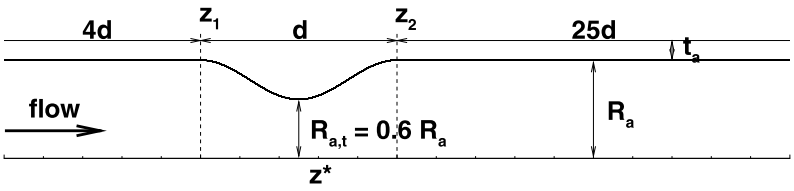

Fig. 3. Sketch (not to scale) of the basic coronary artery geometry: an axisymmetric channel with a stenosis. The blood flow is from left to right. The $R_{a,t}$ indicates the extension of the stenotic region and $z^* = z/d$ is the non-dimensional axial coordinate.

Note that in Eqs. (18) and (19), "⟨⟩" stands for the volume-averaged variables, which is usually adopted for the flow and mass transfer in a porous medium. The diffusion tensor ($\overline{\overline{D}}_E$) is constructed to accommodate the non-isotropic properties of the endothelium such that the diffusion occurs only along the radial direction across the endothelium. The final forms of the continuity and momentum transport equation can be written as [15,29]:

$$\frac{\partial\left(\epsilon\rho_P\langle\vec{v}_E\rangle\right)}{\partial t} + \nabla\cdot\left(\epsilon\rho_P\langle\vec{v}_E\rangle\right) = 0 \tag{20}$$

$$\frac{\partial\left(\epsilon\rho_P\langle\vec{v}_E\rangle\right)}{\partial t} + \nabla\cdot\left(\epsilon\rho_P\langle\vec{v}_E\rangle\langle\vec{v}_E\rangle\right) = -\epsilon\nabla\langle p\rangle + \nabla\cdot\left(\epsilon\mu_P\nabla\langle\vec{v}_E\rangle\right) - \frac{\mu_P\langle\vec{v}_E\rangle}{\overline{\overline{K}}_E} \tag{21}$$

where ρ_P is the density of plasma and μ_P its dynamic viscosity, ϵ is the porosity ($\epsilon = 0$ for the total flow blockage and $\epsilon = 1$ for an entirely free fluid flow), $\langle p\rangle$ is the averaged pressure inside the fluid, $\overline{\overline{K}}_E$ (Eq. (16)) is the non-isotropic permeability of the endothelium tensor, constructed in such a way as to permit only transport in the radial direction.

2.3. Arterial wall: intima, IEL and media

For the rest of the arterial wall (here indicated as "W") that includes the intima, IEL and media, the equations for conservation of mass, momentum and concentration have a similar form to equations presented for the endothelium, with a major difference in assuming the isotropic porous medium and with inclusion of the chemical reaction term within the media to account for the uptake of the LDL by smooth muscle cells there:

$$\frac{\partial\left(\epsilon\rho_P\langle\vec{v}_W\rangle\right)}{\partial t} + \nabla\cdot\left(\epsilon\rho_P\langle\vec{v}_W\rangle\right) = 0 \tag{22}$$

$$\frac{\partial\left(\epsilon\rho_P\langle\vec{v}_W\rangle\right)}{\partial t} + \nabla\cdot\left(\epsilon\rho_P\langle\vec{v}_W\rangle\langle\vec{v}_W\rangle\right) = -\epsilon\nabla\langle p\rangle + \nabla\cdot\left(\epsilon\mu_P\nabla\langle\vec{v}_W\rangle\right) - \frac{\mu_P\langle\vec{v}_W\rangle}{K_W} \tag{23}$$

$$\frac{\partial\langle c_{LDL,W}\rangle}{\partial t} + \left(1-\sigma_f\right)\langle\vec{v}_W\rangle\cdot\nabla\langle c_{LDL,W}\rangle = \nabla\cdot\left(D_W\nabla\langle c_{LDL,W}\rangle\right) - k_{react}\langle c_{LDL,W}\rangle \tag{24}$$

where k_{react} is the biochemical reaction rate coefficient (active only in the media, [14]). To assure continuity of the total transport (convection and diffusion) across the interfaces of individual layers within the arterial wall, we imposed the following boundary condition:

$$\left[\left(1-\sigma_f\right)\langle\vec{v}_W\rangle_n\langle c_{LDL,W}\rangle - D_W\frac{\partial\langle C_{LDL,W}\rangle}{\partial n}\right]\Bigg|_+ = \left[\left(1-\sigma_f\right)\langle\vec{v}_W\rangle_n\langle c_{LDL,W}\rangle - D_W\frac{\partial\langle C_{LDL,W}\rangle}{\partial n}\right]\Bigg|_- \tag{25}$$

where $\langle\vec{v}_W\rangle_n$ is the velocity perpendicular to the interface and where the "+" and "-" indicate the different sides of the interface. To complete the entire system of equations, the porosity, permeability, effective diffusivity and reflection coefficient for each layer are listed in Table 1.

3. Numerical method

The system of the transport equations Eqs. (1)–(3) and (18), (20)–(24) are discretized with a finite-volume based Navier–Stokes solver for complex geometries, within the commercial CFD package ANSYS/Fluent 14.0. Note that a standard version of ANSYS needs to be significantly modified in order to adequately accommodate WSS dependent properties, as well as to include effects of the porous wall structure. This is done by developing a series of user defined functions and user defined variables, which are then integrated with the ANSYS/Fluent solver. The simplified flow chart of the algorithm is shown in Appendix, Fig. 15. The benefits of such an implementation within the commercial CFD code lie in the possibility of direct application of the models developed here to a complex subject or patient specific coronary arteries.

In the present study, all simulations are performed in a steady regime. All diffusive terms of transport equations are discretized by the second-order central differencing scheme (CDS). The quadratic upwind scheme (QUICK) is used for the convective term of the momentum equations. For the discretization of the species (LDL and oxidized LDL), the second-order linear-upwind discretization scheme is applied. Calculation of discretized gradients of all variables is performed by the least squares cell based (LSCB) approach. The SIMPLE algorithm is applied for coupling of the velocity and pressure fields. The final linear set of equations is solved by the algebraic multigrid method (AMG) in combination with the incomplete lower upper (ILU) smoother.

4. Geometry, boundary conditions and numerical mesh

In the present study, we focus primarily on the mathematical aspects of coupling between the blood flow within the lumen and mass transfer of the LDL within the arterial wall. We have selected a simplified axisymmetric geometry of a diseased (stenosed) coronary artery (with a realistic inner radius and thickness of arterial wall of $R_a = 1.85$ mm and $t_a = 0.34$ mm, respectively) that is mathematically well defined and is based on the work of [11], Fig. 3. The total length of the stenotic region is $d = 2R_a$, whereas the entire length of the artery is $L = 30d$. The interface between the lumen and the endothelium within the stenotic region, $z_1 \le z \le z_2$, with $z_1 = 4d$ and $z_2 = 5d$, is described with following function:

$$\frac{r(z)}{R_a} = 1 - \frac{R_a - R_{a,t}}{d}\left\{1 - \cos\left[\frac{2\pi\left(z - z_1 - z_2\right)}{z_2 - z_1}\right]\right\} \tag{26}$$

At later stages of the validation process, in addition to the basic geometry with the stenotic region extension of 40% (i.e. $R_{a,t} = 0.6R_a$), we will also analyze 20% and 60% stenotic extensions (i.e. $R_{a,t} = 0.8R_a$ and $0.4R_a$, respectively), mimicking an earlier and a later stage of atherosclerosis development.

A summary of the applied boundary conditions is shown in Fig. 4. For the blood flow calculations in the lumen, a fully developed and steady laminar parabolic axial velocity profile is applied at the inlet:

$$\left(v_L\right)_z^{IN} = 2V_0\left[1 - \left(\frac{r}{R_a}\right)^2\right] \tag{27}$$

where V_0 is the averaged inlet velocity. In the present study we use $V_0 = 0.24$ m/s to mimic identical flow conditions as presented in [11]

Table 1
Model parameters used in the simulations.

Layer	Symbol	Parameter	Value	Unit	Reference
Lumen	ρ_B	Density	1.0573×10^3	kg/m^3	[14]
	D_L	Diffusivity	2.87×10^{-11}	m^2/s	[14], [30]
	μ_B	Dynamic viscosity	3.70×10^{-3}	kg/m s	[14], [30]
Endothelium	$\overline{\overline{K}}_E$	Permeability	f(WSS), Eq. (16)	m^2	[11], [12]
	$\overline{\overline{D}}_E$	Effective diffusivity	f(WSS), Eq. (17)	m^2/s	[11], [12]
	μ_P	Dynamic viscosity	0.72×10^{-3}	kg/m s	[31]
	σ_f	Reflection coefficient	9.979×10^{-1}	–	[31]
	ϵ	Porosity	5×10^{-5}	–	[32]
Intima	K_W	Permeability	2.00×10^{-16}	m^2	[33]
	D_W	Effective diffusivity	5.40×10^{-12}	m^2/s	[33]
	μ_P	Dynamic viscosity	0.72×10^{-3}	kg/m s	[33]
	σ_f	Filtration coefficient	8.272×10^{-1}	–	[31]
	ϵ	Porosity	9.93×10^{-1}	–	[33]
IEL	K_W	Permeability	4.392×10^{-19}	m^2	[31], [30]
	D_W	Effective diffusivity	3.18×10^{-15}	m^2/s	[31], [30]
	μ_P	Dynamic viscosity	0.72×10^{-3}	kg/m s	[31]
	σ_f	Reflection coefficient	9.827×10^{-1}	–	[31]
	ϵ	Porosity	2×10^{-3}	–	[34]
Media	K_W	Permeability	2.00×10^{-18}	m^2	[33],[35]
	D_W	Effective diffusivity	5.00×10^{-14}	m^2/s	[33],[36]
	μ_P	Dynamic viscosity	0.72×10^{-3}	kg/m s	[31]
	σ_f	Filtration coefficient	8.836×10^{-1}	–	[31]
	ϵ	Porosity	2.58×10^{-1}	–	[37],[30]
	k_{react}	Reaction rate coefficient	3.197×10^{-4}	1/s	[31]

and which closely corresponds to the typical mean velocity in the left coronary artery. At the outlet, a constant pressure is specified with values that correspond to experimental conditions of [38] who performed a series of experiments with pressurized rabbit aorta. As a referent case, the pressure at the outlet was p_{out} = 100 mmHg (13332 Pa), whereas for the hypertension conditions, this value was p_{out} = 150 mmHg (19998 Pa). The pressure at the media/adventitia interface was kept constant at $p_{M/A}$ = 30 mmHg (4000 Pa), which gives values of transmural pressure of 70 and 120 mmHg, respectively, same as in [38]. The symmetry boundary conditions are applied at the center of the axis along the lumen. For the mass transfer of LDL, the inlet and initial values are specified to be $c^0_{LDL} = 3.12$ mol/m^3 (a recommended normal value for an adult person). At the outlet, along the central axis, as well as at radial segments between the lumen and adventitia, a zero gradient boundary condition is applied ($\partial c_{LDL}/\partial n = 0$, where '$n$' indicates the wall-normal direction). To closely mimic experiments of [38], the values of the $c^{M/A}_{LDL}/c^0_{LDL} = 0.005$ and 0.01934, are specified at the media/adventitia (M/A) interface, for the normal and hypertension case, respectively.

Examples of the numerical mesh used are shown in Fig. 5. Note that the numerical mesh in the radial direction is refined in the proximity of the endothelium and the internal elastic layer (IEL). The finest mesh employed 200 control volumes distributed over the stenotic region in the axial direction. In the case of the endothelium resolving simulations, various mesh distributions in the radial direction have been used, varying between 16 and 64 radial segments per endothelium. The mesh convergence study proved that at least 200 axial segments in the stenotic region and 16 radial segments within the endothelium should be used to get the grid independent results (as shown in Appendix and Fig. 14). The numerical mesh in the radial direction is always locally refined in the proximity of all interfaces with a characteristic grid expansion ratio varying between 1.1 and 1.25. The thickness of the very first row of the control volumes next to the lumen/endothelium interface, for various numerical meshes (as listed in Table 2) with N_{end} = 16, 30 and 64, is $r_1/R_a = 10^{-4}, 5\times10^{-5}$ and 2×10^{-5}, respectively.

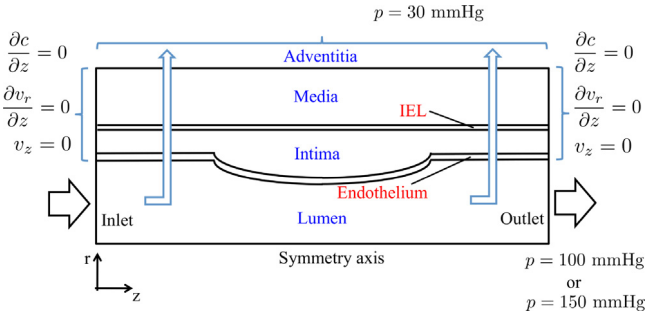

Fig. 4. The sketch of the simulated domain with the imposed boundary conditions.

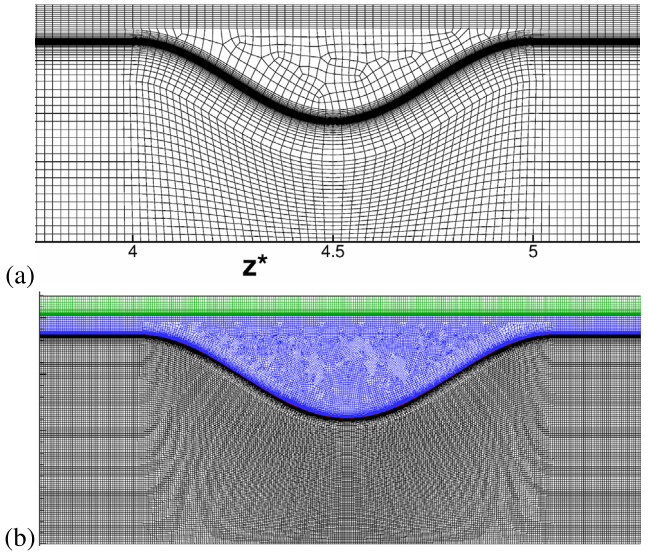

Fig. 5. (a) The coarse numerical mesh in the proximity of the stenotic region used for the endothelium-wall simulations (Model 1); (b) The numerical mesh used for the multilayer-wall simulations (Model 2): lumen (gray), endothelium (black), intima (blue), IEL and media (green).

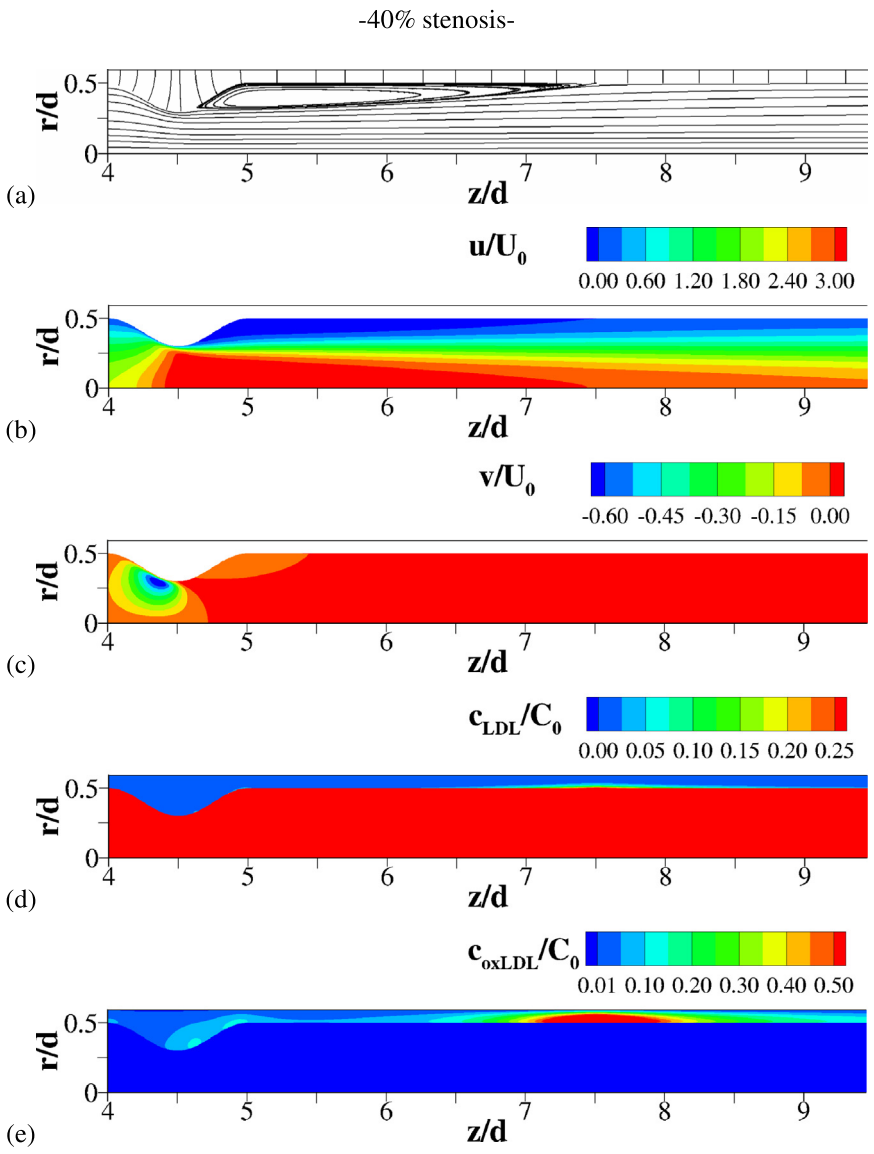

Fig. 6. The simplified coronary artery case with 40% stenosis and transmural pressure of 70 mmHg. All results are obtained with the Model 2 — WSS dependent mass transfer: (a) streamtraces, (b) contours of the non-dimensional streamwise velocity (u/U_0), (c) contours of the non-dimensional radial velocity (v/U_0), (d) contours of the non-dimensional LDL concentration (c_{LDL}/C_0), (e) contours of the non-dimensional oxygenated LDL (c_{oxLDL}/C_0).

Table 2
Model parameters used in the simulations. The 'N' indicates the number of axial (stenosis) and radial (end) segments, whereas 'T' indicates the total number of control volumes per indicated arterial wall region.

	$N_{stenosis}$	N_{end}	T_{lum}	T_{end}	T_{wall}	T_{int}	T_{IEL}	T_{med}
lumen/endothelium								
Mesh A	50	16	$4{\cdot}10^4$	10^4	$3{\cdot}10^4$	–	–	–
Mesh B	50	64	$4{\cdot}10^4$	$4{\cdot}10^4$	$3{\cdot}10^4$	–	–	–
Mesh C	200	16	$2{\cdot}10^5$	$3{\cdot}10^4$	$7{\cdot}10^4$	–	–	–
Mesh D	200	30	$2{\cdot}10^5$	$5{\cdot}10^4$	$8{\cdot}10^4$	–	–	–
Mesh E	200	64	$2{\cdot}10^5$	10^5	$9{\cdot}10^4$	–	–	–
lumen/multi-layered wall								
Mesh F	200	30	$2{\cdot}10^5$	$5{\cdot}10^4$	–	$8{\cdot}10^4$	$4{\cdot}10^3$	$3{\cdot}10^4$

5. Results and discussion

5.1. The models validation was accomplished as follows: the 40% stenosis case and comparative assessment with the "single layer/three pores models" of Olgac et al. [11]

To validate numerical implementation, we start analysis by comparing our results with the model of [11]. As mentioned in the Mathematical model section, this model approximates the entire arterial wall as a single layer, but involves three characteristic pathways for the transport of the LDL from lumen to the arterial wall. This is our reference model (Model 1). In comparison with to this approach, we also develop a more anatomically realistic model of the multi-layered arterial wall (Model 2). Note that both models are identical on the lumen side. The most salient flow and mass transfer features are illustrated in Fig. 6. It can be seen that the blood flow within the lumen exhibits a relatively large recirculation behind the stenosis with characteristic reattachment point at approximately $z^* = 7.5$, Fig. 6(a). The streamtraces within the arterial wall are also present, since the arterial wall is treated as a porous medium. The axial velocity component reaches its peak in the middle of the stenosis and gradually decays farther downstream, Fig. 6(b). A mild variation of the radial velocity component in the lumen is only present at the beginning and the end of the stenotic region, Fig. 6(c). The contours of the non-dimensional concentration of LDL are shown in Fig. 6(d). It can be seen that an enhanced accumulation of the LDL within arterial wall takes place in the proximity of the reattachment

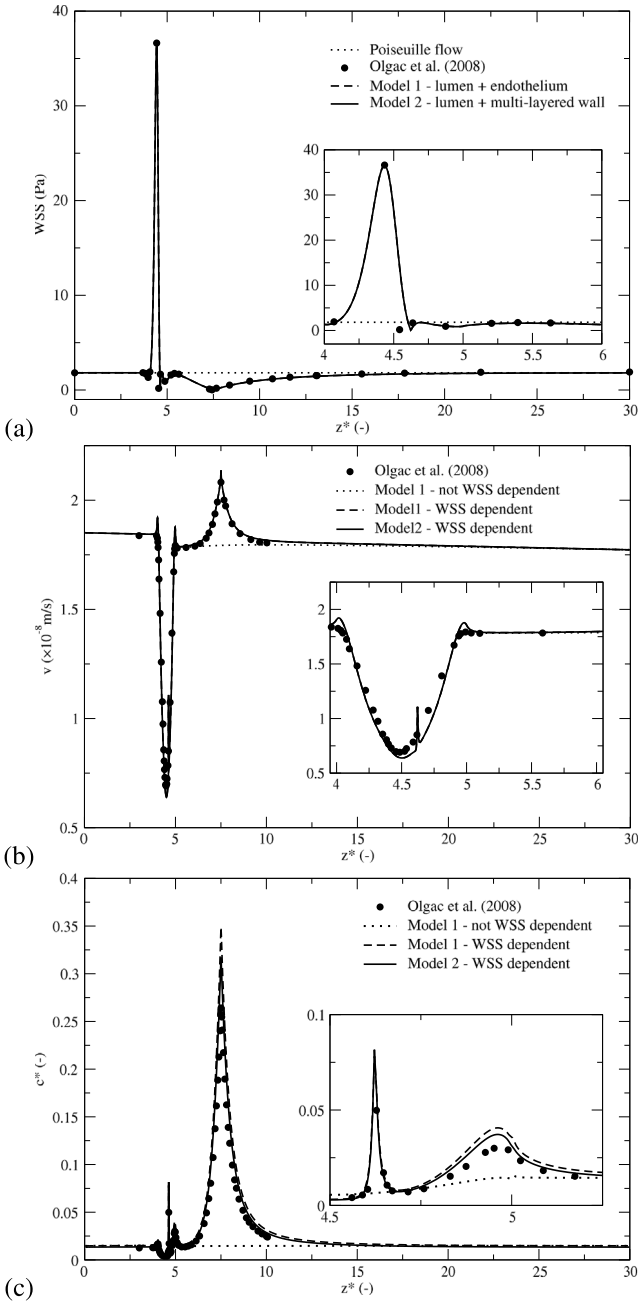

Fig. 7. Profiles of the wall shear-stress (WSS) along the lumen/endothelium interface (a), filtration velocity (b) and non-dimensional LDL concentration ($c^* = c_{LDL}/c_0$) (c) along the endothelium/intima interface for the 40% stenosis case with 70 mmHg transmural pressure.

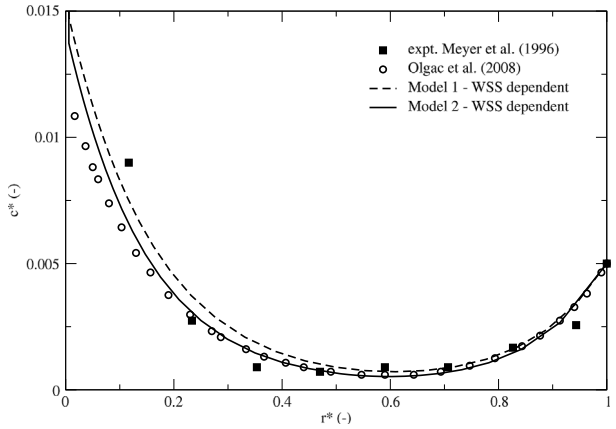

Fig. 8. The radial profiles of the non-dimensional LDL concentration ($c^* = c_{LDL}/c_0$) within the arterial wall extracted at the base point $z^* = 25$. The r^* is the non-dimensional radial distance from the lumen/endothelium interface (normalized by the arterial wall thickness) The simulated case is again artery with 40% stenosis and 70 mmHg transmural pressure, Fig. 4.

point. Note that the discussion of Fig. 6(e), dealing with oxidized LDL, is presented in the last paragraph of Section 5.

To provide a more detailed insight into physics of the lumen/arterial wall interactions, we plot characteristic axial profiles of the absolute wall shear-stress (WSS), the characteristic filtration velocity, and of the non-dimensional LDL concentration (c_{LDL}/c_0) in Fig. 7. The first two are plotted along the lumen/endothelium interface, whereas the latter one is for the endothelium/intima interface. The wall shear-stress reaches its peak in the proximity of the center of the stenosis, later equals zero at the reattachment point ($z/d = 7.5$), and finally, turns back to the undisturbed values (the Poiseuille solution) after $z/d = 25$, Fig. 7(a). It can be seen that the present simulations are in good agreement with the results of [11], also confirming the adequacy of the numerical mesh employed. The filtration velocity exhibits more complex behavior, as shown in Fig. 7(b). The local minimum is reached in the stenosis center, followed with local maxima at the separation ($z^* = 4.625$) and reattachment ($z^* = 7.5$) points (for the wall shear-stress dependent properties, Model (2)). These peaks are not present in the models with constant transport properties. The profiles of the non-dimensional concentration (c_{LDL}/c_0), for the models with the WSS-dependent properties, extracted along the endothelium/intima interface, exhibit characteristic peaks at the beginning and the end of stenosis, as well as at separation and reattachment points, Fig. 7(c). The models with the WSS-dependent transport properties are portraying a dramatic increase of the LDL concentration (up to 35% of the value within the lumen) within the arterial wall at locations where the WSS is zero. At these locations, the mass transfer through the leaky junctions is largest (due to reduced flow and mass transfer resistance), causing an increase in the overall mass transfer. By further zoom-in in the proximity of the separation pint ($z^* = 4.625$, Fig. 7(c)), we can directly compare the levels of the non-dimensional concentration of LDL (c^*) for the a standard (not WSS dependent model) (Model 1) and WSS dependent models (Model 2). At this particular location approximately a ten-fold increase is obtained with the WSS dependent properties, stressing importance of considering this effect. It can be also seen that there is a strong correlation with the filtration velocity distribution and that a good agreement is obtained with the results of [11], confirming a proper implementation of the three-pore model.

The radial profile of the non-dimensional LDL concentration extracted at $z^* = 25$ is shown in Fig. 8. As can be seen in Fig. 7, at this particular location, both blood flow and mass transfer are reaching their undisturbed values. This location is selected to mimic the experimental conditions of [38] with pressurized rabbit aorta. The simulated values are in a qualitatively good agreement with the measured values. Note that the characteristic distribution of the LDL concentration with a local minimum around $r^* = 0.6$ is caused by activation of the biochemical reaction term, which simulate the uptake of LDL by the smooth muscle cells within the media. It can also be seen that the present models show a better agreement with experiments in the proximity of the endothelium ($r^* = 0.1$) compared to the model of [11]. This improvement can be explained because of a more realistic geometrical representation of the multi-layered arterial wall, in contrast to a single homogeneous layer, as was used in [11].

5.2. Effects of hypertension

As a next step, the model response will be analyzed by imposing an increased transmural pressure of 120 mmHg, which mimics

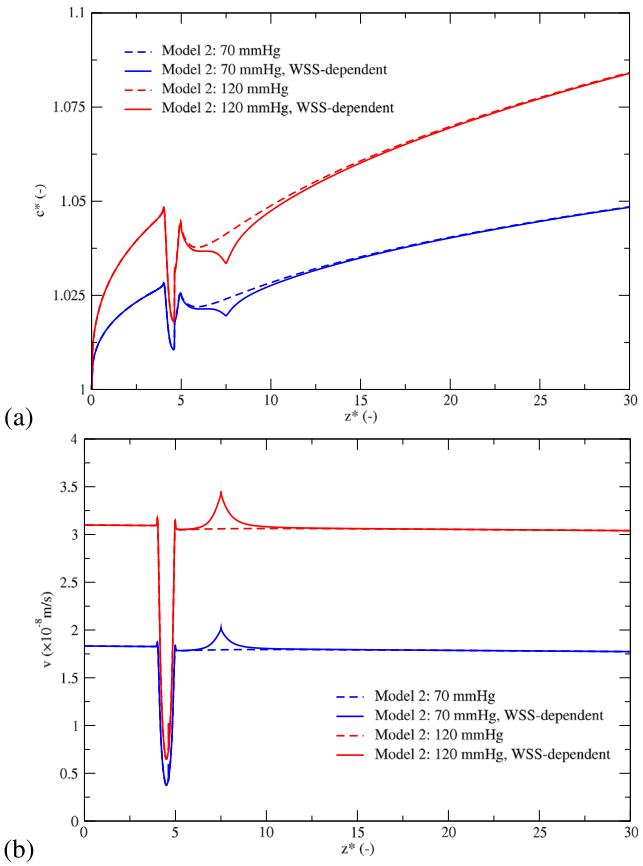

Fig. 9. The non-dimensional concentration of LDL ($c^* = c_{LDL}/c_0$) (a) and the filtration velocity (b) along the lumen/endothelium interface of the coronary artery with 40% stenosis for two different values of the applied transmural pressure of 70 mmHg and 120 mmHg, respectively.

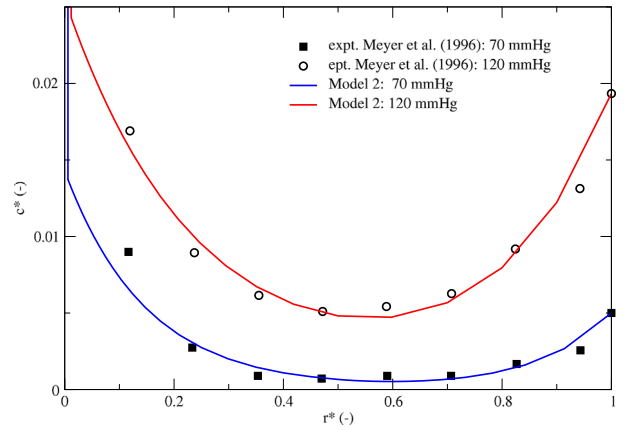

Fig. 10. The radial profile of the non-dimensional concentration of LDL ($c^* = c_{LDL}/c_0$) within the arterial wall of the coronary artery with 40% stenosis for two values of the transmural pressure of 70 mmHg and 120 mmHg, respectively.

hypertension. This is achieved by increasing the pressure at the lumen outlet to 150 mmHg, whereas the pressure at the intima/media interface was kept constant at 30 mmHg. The characteristic axial profiles of the non-dimensional LDL concentration (c_{LDL}/c_0), along the lumen/endothelium interface, are shown in Fig. 9(a). Note that the mechanism of concentration polarization (an increase of the LDL concentration in the proximity of the arterial wall compared to its initial value) can be observed. This behavior is due to a higher mass transfer resistance imposed by the endothelium, which is treated as a porous layer, is previously also reported in [14,15,39–46]. The differences between models with constant and WSS-dependent transport properties are present only in the region after stenosis, where WSS-dependent profiles exhibit a local minimum at the reattachment point. This is explained in view of a LDL transfer increase through the leaky junctions. Additionally, both models have a characteristic drop within the stenosis region ($4 \leq z^* \leq 6$) caused by a strong blood flow acceleration in the axial direction followed by a sudden drop in the filtration velocity, Fig. 9(b). It can be seen that the elevated transmural pressure produces overall larger polarization of the LDL along the lumen/endothelium interface, Fig. 9(a). Similarly, the filtration velocity shows a significant increase in undisturbed regions, from a 1.8×10^{-8} to 3.1×10^{-8} m/s. Note that at the reattachment point, characteristic peaks in the filtration velocity can be observed (due to already mentioned reduced endothelial resistance, when WSS is low).

To get insights into the LDL concentration distribution inside the arterial wall, the radial profiles extracted at an undisturbed location ($z^* = 25$) are shown in Fig. 10. A qualitatively good agreement is obtained between simulations and experiments. Hypertension causes significantly higher levels of the non-dimensional LDL concentration inside the arterial wall. For example, by comparing the values at the center of the media ($r^* \approx 0.6$,) where the lowest values are obtained), it can be seen that an almost tenfold increase in the LDL concentration is observed, i.e. c_{LDL}/c_0 reach 5×10^{-4} and 4.7×10^{-3}, for transmural pressures of 70 mmHg and 120 mmHg, respectively. At the media/adventitia interface ($r^* = 1$), this enhancement is still significant, with a fourfold increase.

5.3. Effect of changing the stenotic regions: 20% and 60% stenosis cases

Next, we analyze the effect of changing the severity of stenosis by introducing a less (20% radius reduction) and more advanced (60% radius reduction) stages of atherosclerosis – under identical transmural pressure of 70 mmHg – as previously done for the reference case of 40% arterial intima reduction. It can be seen that the geometrical impact on flow and mass transfer is significant, as shown in Figs. 11 and 12. For the 20% radius reduction case, the flow recirculation is hardly visible and is confined to the very narrow region in the proximity of the stenosis ending (at $z^* = 5$), Fig. 11(a). In contrast, for the 60% radius reduction case, a very long recirculation region is generated with the reattachment point located at $z^* = 18$ (compared to $z^* = 7.5$ for the 40% radius reduction case), Fig. 12(a). Also, from contours of the non-dimensional axial and radial velocity, it is concluded that smaller stenosis imposed a relatively small and larger stenosis imposed a massive alteration of both axial and radial velocity, and, significantly extended disturbed region, Figs. 11(b),(c) and 12(b),(c). This alteration of the blood flow patterns has a pronounced influence on the distribution of the LDL concentration along and inside the arterial wall, Figs. 11(d) and 12(d). To analyze these variations in more details, we plot profiles of the wall shear-stress, filtration velocity and LDL concentrations along the lumen/endothelium and endothelium/intima interfaces, Fig. 13. From the WSS profiles, distinct separation points can be identified at $z^* = 4.8175$, 4.6255 and 4.5675 for the 20%, 40% and 60% stenosis cases, respectively. Similarly, the reattachment points are located at $z^* = 5.0225$, 7.5 and 18, respectively. From profiles of the filtration velocity, Fig. 13(b), it is shown that the local peaks coincide with reattachment and separation points. Consequently, this behavior is also mirrored in distributions of the non-dimensional LDL concentration, Fig. 13(c). This also explains the local accumulation of the LDL concentration for the 20% stenosis case, shown in contour plots in Fig. 11(d), i.e. due to flow reattachment location in the proximity of the stenosis ending. It is interesting to note that the peak values of c_{LDL}/c_0 are very similar for all cases. This is because of the identical value of the transmural pressure (70 mmHg) for all geometries.

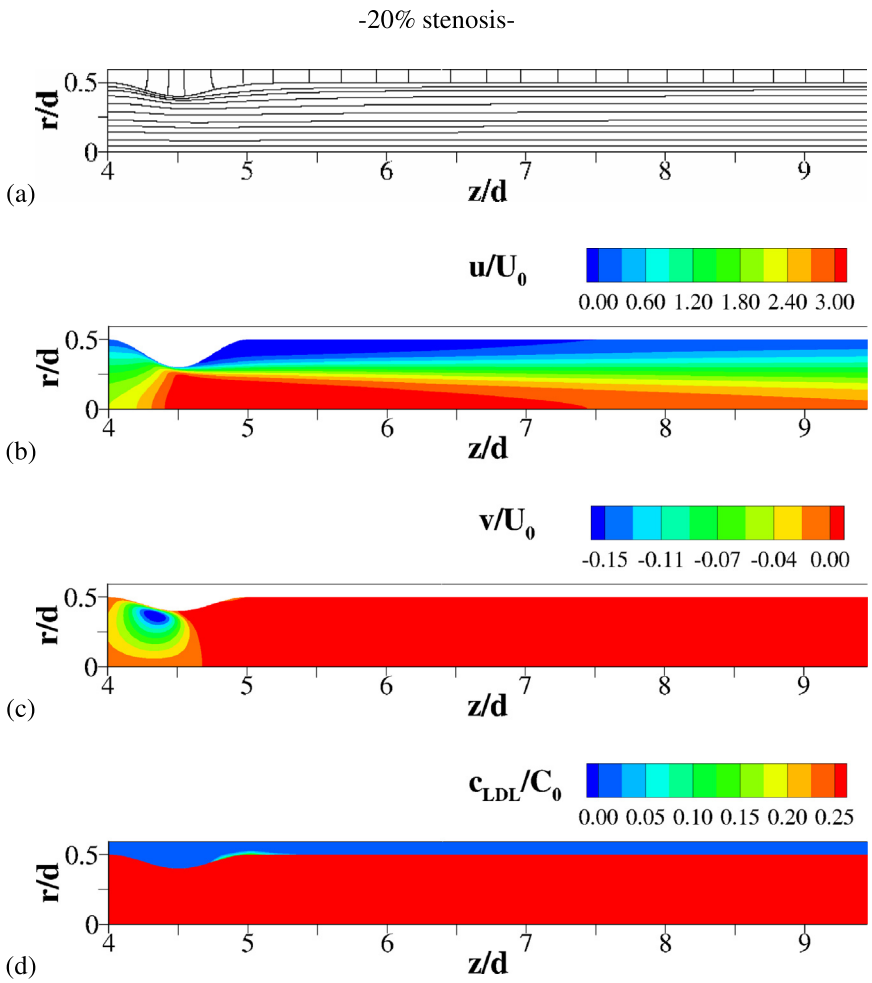

Fig. 11. The simplified coronary artery with 20% stenosis and transmural pressure of 70 mmHg. The streamtraces (a), the contours of the non-dimensional streamwise (u/U_0) (b) and radial (v/U_0) (c) velocity, and the non-dimensional concentration of LDL ($c^* = C_{LDL}/C_0$) (d).

5.4. Modeling of inflammation: oxidized LDL (oxLDL) distribution

In addition to the transport of LDL within the arterial wall, we also made a first step towards modeling of the inflammatory process within the arterial wall. This is done by solving the transport equation of the oxidized LDL, which has the following form:

$$\frac{\partial \langle c_{\mathrm{oxLDL,W}} \rangle}{\partial t} + \left(1-\sigma_f\right) \langle \vec{v}_{\mathrm{W}} \rangle \cdot \nabla \langle c_{\mathrm{oxLDL,W}} \rangle = \nabla \cdot \left(D_{\mathrm{W}} \nabla \langle c_{\mathrm{oxLDL,W}} \rangle \right) + \mathcal{R}^{\mathrm{react}}_{\mathrm{oxLDL}} \tag{28}$$

where $\mathcal{R}^{\mathrm{react}}_{\mathrm{oxLDL}}$ is the source term due to oxidation of LDL, which is represented as an irreversible first-order biochemical reaction, i.e. $\mathcal{R}^{\mathrm{react}}_{\mathrm{oxLDL}} = d_{\mathrm{LDL}} \langle c_{\mathrm{LDL,w}} \rangle$, with $d_{\mathrm{LDL}} = 3 \times 10^{-4}$ 1/s, as measured by [47] and used in [48]. The major source contribution to the oxidized LDL comes from a local concentration of the LDL, i.e. the most active oxidation will occur at the locations inside the arterial wall with elevated levels of LDL. It should be noted that the present model of LDL oxidation is a very simple one, introduced here just to conceptually validate a proof of concept for a possible model of inflammation. The more advanced model includes detailed biochemical reactions which involve the monocytes and macrophages as an immune response to an already initiated inflammation process, [48,49]. The results obtained for calculated concentrations of the oxidized LDL are shown in Fig. 6(e). It can be seen that oxidized LDL is confined within the arterial wall at locations where the concentration of the LDL is highest, i.e. in the proximity of the reattachment point as well as in the stenosis region where the separation occurs. These are locations most affected by the inflammation. The present distribution is qualitatively very similar to obtained concentrations for oxidized LDL presented in [48], confirming the validity of the present approach.

6. Potential clinical benefits

The potential clinical befits of the present study can be in application of the developed CFD tool for a recognition of the initial (or advanced) stage of the atherosclerosis. The present model can be applied for the patient specific geometries obtained from the CT/MRI scans (similar to Fig. 1) with measured levels of the LDL concentration in the blood sample. The model can be run for the measured values of the transmural pressure (variations of the measured value). In addition to the map of the WSS at the lumen/endothelium interface, the highest local levels of the LDL and oxidized LDL inside the arterial wall can be easily visualized indicating regions with an active inflammation.

7. Limitations of the present study

The arterial wall is assumed to be rigid, i.e. possible fluid–structure interaction (FSI) effects were not considered. The thickness of the arterial wall (except the intima sublayer) is assumed to be constant. The glycocalyx layer is neglected, but the current model is directly applicable under the assumption that the this layer is already removed and that lumen is in direct contact with the endothelium. The modeling of inflammation is based on a very simple transport equation of the oxidized LDL. This needs to be extended with a more comprehensive

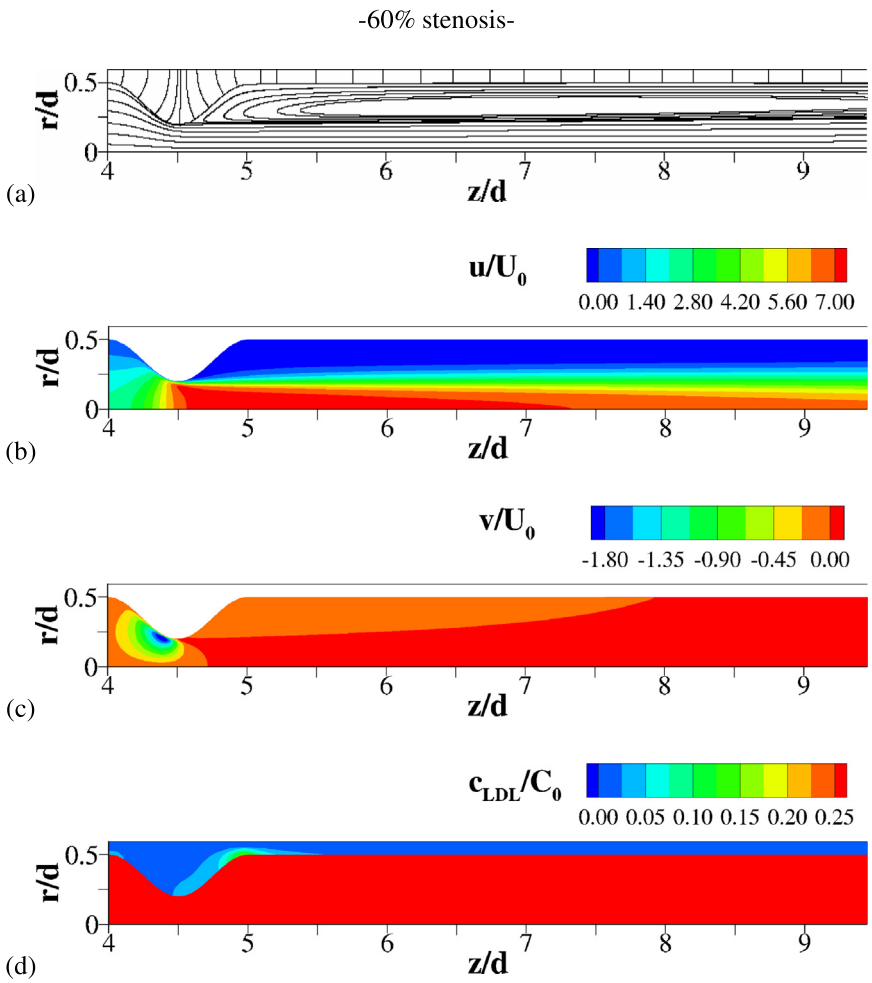

Fig. 12. Same as in the previous figure, only now for the 60% stenosis case.

model which, in addition to LDL and oxLDL, also includes transport of monocytes, macrophages, foam cells, smooth muscle cells, cytokines, and collagen. The performed simulations are done in a steady mode. The pulsating inflow conditions can be easily adopted in future studies. Finally, the considered geometry is based on an exact mathematical distribution function, whereas the patient-specific geometries will be more complex.

8. Summary and conclusions

A comprehensive model of coupled blood flow and LDL transfer through the arterial wall is presented. The arterial wall is considered as a multi-layered porous structure with distinct transport properties for each sublayer: endothelium, intima, internal elastic layer (IEL) and media. Our particular focus is the endothelial layer, which is a first interface between the lumen and the arterial wall. Here, three primary mechanisms of the transfer of LDL are considered: the normal and leaky junctions and the vesicular pathway. This is done through expressing the endothelium transport properties as a function of the wall shear-stress at the lumen side. The present contribution represents a novel approach combining treatment of the multi-layered arterial wall structure and the multipore modeling of the mass transfer of LDL. The present models are extensively validated for cases involving a simplified axisymmetric geometry with a stenosis of different severities. The wall shear-stress dependent transport properties of the endothelium are the most important in the proximity of the separation and reattachment regions. Compared to the models with constant properties, the local increase of the LDL concentration along the endothelium/intima interface can be as much as tenfold. Also, the effects of hypertension are analyzed. For all cases considered, a qualitatively good agreement is obtained with available results in the literature, which include the numerical and modeling studies, as well as measurements in rabbit aorta. The present models show improvements in predicting the LDL concentration in the proximity of the endothelium. Particularly important are results indicating a significant (between two and ten times) increase of the local LDL concentration at particular locations inside the arterial wall, caused by elevated pressure (hypertension effect). A very preliminary attempt to model the inflammatory process within the arterial wall by solving a governing equation for the oxidized LDL is presented too. By visualizing contours of the oxidized LDL, locations where inflammation occurs are identified. These regions show a great s the similarity with results of more detailed models of inflammation reported in the literature. The present multipore/multilayer model is recommended for use as a basic modeling platform for future studies dealing with the initial onset of atherosclerosis as well as its progression.

Declaration of competing interest

The authors declare that they have no conflict of interest.

Acknowledgments

Dr. T. van Walsum and Dr. H. A. Kirisli, Erasmus Medical Centre Rotterdam, The Netherlands, are acknowledged for providing Fig. 1.

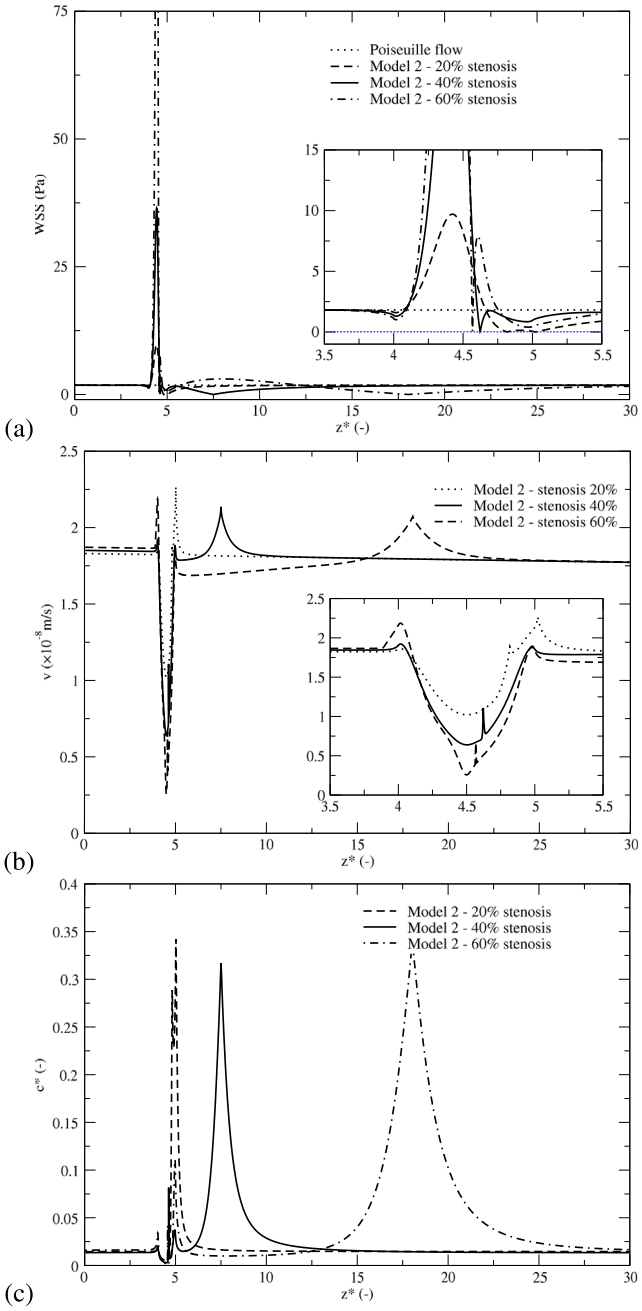

Fig. 13. The profiles of the WSS along the lumen/endothelium interface (a), filtration velocity (b) and non-dimensional LDL concentration (c_{LDL}/c_0) (c) along the endothelium/intima interface for different levels of stenosis: 20, 40 and 60%, respectively.

Appendix

To check the mesh dependency in more details, we have selected to analyze the filtration velocity profiles along the endothelium/intima interface, since it is one of the most sensitive quantities. The mesh convergence study proved that at least 200 axial segments in the stenotic region and 16 radial segments within the endothelium should be used to get the grid independent results, Fig. 14. This is additionally confirmed by analyzing the WSS profiles (extracted along the lumen/endothelium) where an excellent agreement is obtained in comparison with characteristic peak values of [11], as shown in Fig. 7.

The WSS-dependent properties in the endothelium are implemented with several user defined functions (UDF). 'determine_proximity.c'

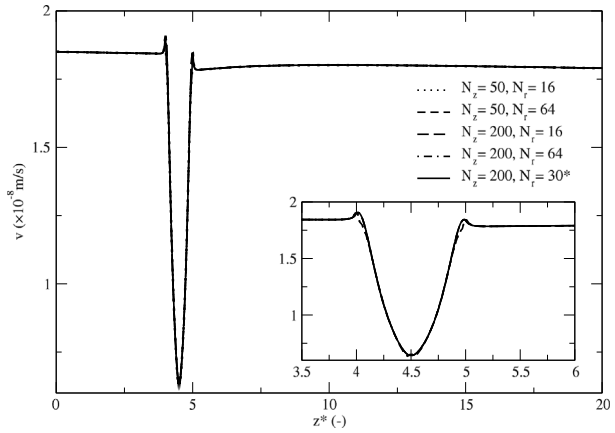

Fig. 14. Mesh dependence of the filtration velocity profile (at the endothelium/intima interface).

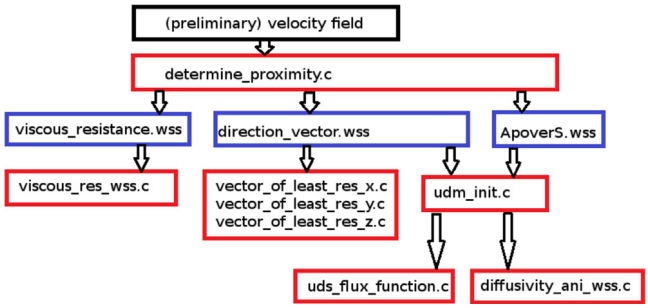

Fig. 15. Schematic representation of information transfer from the velocity field to the different wall shear-stress dependent properties in the endothelium. Red boxes indicate the user defined functions (UDFs) which are written separately in the C-program language and coupled with the Fluent/ANSYS; the blue boxes are additional variables (data files).

is an execute-on-demand UDF. It determines for every computational cell inside the endothelium which cell face at the lumen/endothelium interface is closest. The WSS is calculated at that face, from which several WSS-dependent quantities are derived and written in files. The values of $\overline{K}_E$ from Eq. (15) for each cell are written in 'viscous_resistance.wss' and are read out by another UDF to implement the WSS-dependent viscous resistance in Fluent. The A_P/S from Eq. (9) is saved in 'ApoverS.wss' and is used by UDFs to implement the WSS-dependent diffusivity and reflection coefficient of LDL. The unit normal vector of the cell face is saved in 'direction_vector.wss' which is used for both the anisotropic viscous resistance and the anisotropic diffusivity of LDL.

References

[1] C.D. Mathers, A. Lopez, C. Stein, D. Ma Fat, C. Rao, M. Inoue, K. Shibuya, N. Tomijima, C. Bernard, H. Xu, Deaths and disease burden by cause: Global burden of disease estimates for 2001 by world bank country groups, in: WHO Disease Control Priorities Project Working Paper, vol. 18, 2005.

[2] V.L. Roger, A.S. Go, D.M. Lloyd-Jones, R.J. Adams, J.D. Berry, T.M. Brown, M.R. Carnethon, S. Dai, G. de Simone, E.S. Ford, et al., Heart disease and stroke statistics 2011 update, a report from the American Heart Association, Circulation 123 (4) (2011) e18–e209.

[3] G.A. Roth, et al., Global, regional and national burden of cardiovascular diseases for 10 causes, 1990 to 2015, J. Am. Coll. Cardiol. 70 (1) (2017) 1–25.

[4] E. Wilkins, L. Wilson, K. Wickramasinghe, P. Bhatnagar, J. Leal, R. Luengo-Fernandez, R. Burns, M. Rayner, N. Townsend, European cardiovascular disease statistics 2017. European Heart Network, Brussels, 2017.

[5] F.H. Epstein, R. Ross, Atherosclerosis is an inflammatory disease, New Engl. J. Med. 340 (2) (1999) 115–126.

[6] P. Libby, P.M. Ridker, A. Maseri, Inflammation and atherosclerosis, Circulation 105 (2002) 1135–1143.
[7] A. Maton, Human biology and health, Prentice Hall, Englewood Cliffs, N.J, 1997.
[8] G.A. Truskey, F. Yuan, D.F. Katz, Transport Phenomena in Biological Systems, second ed., Pearson Prentice Hall Bioengineering, 2009.
[9] S. Wada, M. Koujiya, T. Karino, Theoretical study of the effect of local flow disturbances on the concentration of low-density lipoproteins at the luminal surface of end-to-end anastomosed vessels, Med. Biol.Eng. Comput. 40 (5) (2002) 576–587.
[10] J.V. Soulis, D.K. Fytanidis, V.C. Papaioannou, G.D. Giannoglou, Wall shear stress on LDL accumulation in human RCAs, Med. Eng. Phys. 32 (2010) 867–877.
[11] U. Olgac, V. Kurtcuoglu, D. Poulikakos, Computational modeling of coupled blood-wall mass transport of LDL: effects of local wall shear stress, Am. J. Physiolo. Heart. Circ. Physiol. 294 (2008) H909–H919.
[12] U. Olgac, D. Poulikakos, S.C. Saur, H. Alkadhi, V. Kurtcuoglu, Patient-specific three-dimensional simulation of LDL accumulation in a human left coronary artery in its healthy and atherosclerotic states, Am. J. Physiol. - Heart Circ. Physiol. 296 (2009) H1969–H1982.
[13] D.G. Mpairaktaris, J.V. Soulis, G.D. Giannoglou, Low density lipoprotein transport through patient-specific thoracic arterial wall, Comput. Biol. Med. 89 (2017) 115–126.
[14] N. Yang, K. Vafai, Modeling of low-density lipoprotein (LDL) transport in the artery-effects of hypertension, Int. J. Heat Mass Transfer 49 (5) (2006) 850–867.
[15] L. Ai, K. Vafai, A coupling model for macromolecule transport in a stenosed arterial wall, Int. J. Heat Mass Transfer 49 (2006) 1568–1591.
[16] S. Chung, K. Vafai, Effect of the fluid–structure interactions on low-density lipoprotein transport within a multi-layered arterial wall, J. Biomech. 45 (2012) 371–381.
[17] K. Jesionek, M. Kostur, Effects of shear stress on low-density lipoproteins (LDL) transport in the multi-layered arteries, Int. J. Heat Mass Transfer 81 (2015) 122–129.
[18] M. Roustaei, M.R. Nikmaneshi, B. Firoozabadi, Simulation of low density lipoprotein (LDL) permeation into multilayer corronary arterial wall: Interactive effects of wall shear stress and fluid–structure interaction in hypertension, J. Biomech. 67 (2018) 114–122.
[19] J.M. Tarbell, Shear stress and the endothelial transport barrier, Cardiovasc. Res. 87 (2010) 320–330.
[20] L.M. Cancel, A. Fitting, J.M. Tarbell, In vitro study of LDL transport under pressurized (convective) conditions, Am. J. Physiol. Heart Circ. Physiol. 293 (2007) H126–H132.
[21] F. Curry, Mechanics and thermodynamics of transcapillary exchange, in: Handbook of Physiology, Vol. 4, 1984, pp. 309–374, Part 1.
[22] S. Weinbaum, G. Tzeghai, P. Ganatos, R. Pfeffer, S. Chien, Effect of cell turnover and leaky junctions on arterial macromolecular transport, Am. J. Physiol. -Heart Circ. Physiol. 248 (6) (1985) H945–H960.
[23] M.J. Levesque, D. Liepsch, S. Moravec, R.M. Nerem, Correlation of endothelial-cell shape and wall shear-stress in a stenosed dog aorta, Arteriosclerosis 6 (1986) 220–229.
[24] A. Suciu, Effects of External Forces on Endothelial Cells (Ph.D. thesis), EPFL, Switzerland, 1997.
[25] J.J. Chiu, D.L. Wang, S. Chien, R. Skalak, S. Usami, Effects of disturbed flow on endothelial cells, J. Biomech. Eng-T ASME 120 (1998) 2–8.
[26] N. Sakamoto, T. Ohashi, M. Sato, Effect of shear stress on permeability of vascular endothelial monolayer cocultured with smooth muscle cells, JSME Int. J. Ser. C Mech. Syst. 47 (2004) 992–999.
[27] S. Chien, Molecular and mechanical bases of focal lipid accumulation in arterial wall, Prog. Biophys. Mol. Bio. 83 (2003) 131–151.
[28] S.J. Lin, K.M. Jan, S. Weinbaum, S. Chien, Transendothelial transport of low-density lipoprotein in association with cell mitosis in rat aorta, Arteriosclerosis 9 (1989) 230–236.
[29] K. Vafai, C.L. Tien, Boundary and inertia effects on flow and heat transfer in porous media, Int. J. Heat Mass Transfer 24 (1981) 195–203.
[30] G. Karner, K. Pertkold, H.P. Zehentner, Computational modeling of macro-molecule transport in the arterial wall, Comput. Methods Biomech. Biomed. Eng. 4 (6) (2001) 491–504.
[31] M. Prosi, P. Zunino, K. Perktold, A. Quarteroni, Mathematical and numerical models for transfer of low-density lipoproteins through the arterial walls: A new methodology for the model set up with applications to the study of disturbed lumenal flow, J. Biomech. 38 (4) (2005) 903–917.
[32] S.J. Lin, G. Schuessler, S. Weinbaum, S. Chien, Enhanced macro-molecular permeability of aortic endothelial cells in association with mitosis, Atherosclerosis 73 (2) (1988) 223–232.
[33] Y. Huang, D. Rumschitzki, S. Chien, S. Weinbaum, A fiber matrix model for the growth of macromolecular leakage spots in the arterial intima, J. Biomech. Eng. 116 (1994) 430–445.
[34] S.H. Song, M.R. Roach, Quantitative changes in the size of fenestration of elastic laminas of sheep thoracic aorta studied with SEM, Blood Vessels 20 (1983) 145–153.
[35] C.B. Vargas, F.F. Vargas, J.G. Pribyl, P.L. Blackshear, Hydraulic conductivity of the endothelial and outer layers of the rabbit aorta, A. J. Physiol. 236 (1979) H53–H60.
[36] G.A. Truskey, W.L. Roberts, R.A. Herrmann, R.A. Malinauskas, Measurement of endothelium permeability to^{125}I-low density lipoproteins in rabbit arteries by use of en face preparations, Circ. Res. 71 (1992) 883–897.
[37] Z.J. Huang, J.M. Tarbell, Numerical simulation of mass transfer in porous media of blood vessel walls, Am. J. Physiol. 273 (1997) H464–H477.
[38] G. Meyer, R. Merval, A. Tedgui, Effects of pressure-induced stretch and convection on low-density lipoprotein and albumin uptake in the rabbit aortic wall, Circ. Res. 79 (3) (1996) 532–540.
[39] N. Fatouraee, X. Deng, A. De Champlain, R. Guidoin, Concentration polarization of low density lipoprotein (LDL) in the arterial system, Ann. New York Acad. Sci. 858 (1998) 137–146.
[40] S. Wada, T. Karino, Theoretical study on flow-dependent concentration polarization of low density lipoproteins at the luminal surface of a straight artery, Biorheology 36 (1999) 207–223.
[41] Z. Ding, Y. Fan, X. Deng, Effect of LDL concentration polarization on the uptake of LDL by human endothelial cells and smooth muscle cells co-cultured, Acta Biochim. Biophys. Sin. 41 (2) (2009) 146–153.
[42] X. Liu, F. Pu, Y. Fan, X. Deng, D. Li, S. Li, A numerical study on the flow of blood and the transport of LDL in the human aorta: The physiological significance of the helical flow in the aortic arch, Am. J. Physiol. Heart. Circ. Physiol. 297 (2009) H163–H170.
[43] X. Liu, Y. Fan, X. Deng, Effect of the endothelial glycocalyx layer on arterial LDL transport under normal and high pressure, J. Theoret. Biol. 283 (1) (2011) 71–81.
[44] S. Kenjereš, A. de Loor, A modeling and simulation of low-density-lipoprotein (LDL) transport through multi-layered wall of an anatomically realistic carotid artery bifurcation, J. R. Soc. Interface 11 (91) (2014) 1–13, 2013094.
[45] M. Iasiello, K. Vafai, A. Andreozzi, N. Bianco, F. Tavakkoli, Effects of external and internal hyperthermia on LDL transport and accumulation within an arterial wall in the presence of a stenosis, Ann. Biomed. Eng. 43 (7) (2015) 1585–1599.
[46] S. Kenjereš, On recent progress in modelling and simulations of multi-scale transfer of mass, momentum and particles in bio-medical applications, Flow Turbul. Combust. 96 (3) (2016) 837–860.
[47] H. Esterbauer, G. Striegl, H. Puhl, M. Rothheneder, Continuous monitoring of in vitro oxidation of human low density lipoprotein, Free Radic. Res. Commun. 6 (1989) 67–75.
[48] M. Cilla, E. Pena, M.A. Martinez, Mathematical modelling of atheroma plaque formation and development in coronary arteries, J. R. Soc. Interface 11 (2014) 1–16, 20130866.
[49] V. Calvez, A. Ebde, N. Meunier, A. Raoult, Mathematical modelling of the atherosclerotic plaque formation, ESAIM Proc. EDP Sci. 28 (2009) 1–12.